CONFERENCE PRE-PRINT

3D MODELLING OF THERMAL LOADS DURING UNMITIGATED VERTICAL DISPLACEMENT EVENTS IN ITER AND JET

F.J. ARTOLA, R.A. PITTS, I.S. CARVALHO, G. SIMIC, A. LOARTE ITER Organization
St. Paul-lez-Durance, France
Email: javier.artola@iter.org

S.N. GERASIMOV United Kingdom Atomic Energy Authority Abingdon, United Kingdom

A. REDL Max Planck Institute for Plasma Physics Garching, Germany

M. KONG Ecole Polytechnique Federal de Lausanne Lausanne, Switzerland

Abstract

Predicting three-dimensional thermal loads during tokamak disruptions is essential for ITER yet remains weakly developed. We present a physics-based workflow that couples MHD simulations of vertical displacement events with field-line tracing on a realistic 3D first-wall model and a transient wall thermal response. The approach is validated against JET discharges with beryllium main chamber armour, reproducing key global dynamics, non-axisymmetric current features, and the occurrence (or absence) of melting, thereby building confidence in the methodology. We then apply the same workflow to ITER-relevant conditions with tungsten armour, consistent with the new 2024 ITER re-baseline, to assess disruption heat loads and their 3D localization. The analysis highlights the impact of the 3D wall geometry and MHD induced toroidal asymmetries and broadening of the energy deposition profile. Beyond these studies, the workflow enables scenario-by-scenario estimates of disruption-induced thermal loading, allowing to assess the disruption-budget consumption for these events in future devices.

1. INTRODUCTION

The modelling of 3D thermal loads during tokamak disruptions remains largely unexplored, with no reliable predictive tools for future machines. During the Thermal Quench (TQ) and Current Quench (CQ) phases of disruptions at high plasma currents, the rapid loss of thermal and magnetic energy can cause severe melting of plasma-facing components (PFC), leading potentially to extremely costly operational delays, especially in nuclear devices. Predictive, and as realistic as possible modelling tools, are therefore essential to establish disruption mitigation needs and assess the disruption budget for next step tokamaks.

Previous work for ITER CQ loads during upward-going, unmitigated vertical displacement events (VDE) on the beryllium (Be) main chamber PFCs of the ITER 2016 Baseline configuration was performed with the DINA–SMITER–MEMOS-U workflow [1]. There, melting was predicted already for plasma currents $I_p > 7.0$ MA, and with severe melt erosion for nominal 15 MA operation. The new ITER 2024 baseline replaces Be by tungsten (W) as main chamber armour [2], which considerably increases melt limits. Nevertheless, axisymmetric TOKES simulations of the same VDE CQ still predict melting onset for $I_p \approx 10$ MA in W [3]. Although the study in [1] did account for the 3D geometry of the ITER first wall panels (FWP) and the temporal evolution of the CQ equilibrium, the use of the 2D DINA code required that the plasma parallel heat flux (q_{\parallel}) , be assumed toroidally symmetric. The TOKES calculations are also axisymmetric and account for neither the 3D wall structure nor the magnetic equilibrium time variation. Since the edge safety factor (q_{95}) during such CQs typically drops below a

value of 2, external kink modes are expected to be triggered, breaking the axisymmetry assumption and leading to strong, time dependent toroidal asymmetries in q_{\parallel} . Therefore, both DINA and TOKES simulations are expected to underestimate the localization of thermal loads and it is imperative to assess the impact of 3D plasma effects.

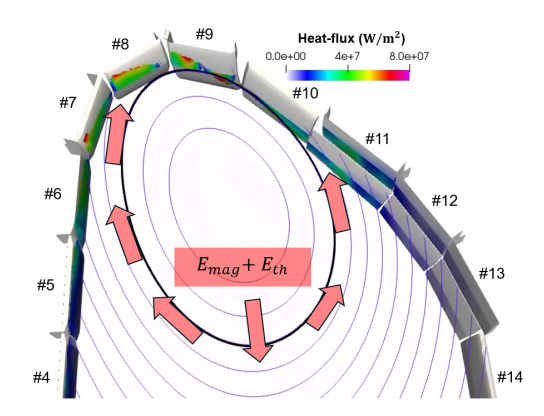


FIG. 1. Example of an ITER CQ simulation with JOREK (see section 4) together with the FWP indexing and the perpendicular heat fluxes on the FW. The equilibrium is taken at t = 0.391 s with $q_{95} = 1.77$.

In this article, we report, for the first time, JOREK simulations of unmitigated VDE heat loads which account for 3D plasma loads and a realistic wall geometry. Using the first-principles methodology described in Section 2, we simulate two dedicated upward-going VDEs in JET and validate the predicted thermal and current loads in Section 3. This successful validation increases confidence in the model and motivates its application to ITER, where we perform equivalent simulations and analyse the resulting thermal loads (Section 4). Finally, Section 5 summarizes the main findings and outlines directions for future work.

2. METHODOLOGY AND MODEL ASSUMPTIONS

The workflow employed to compute disruption-induced thermal loads proceeds in three stages. First, nonlinear resistive-MHD simulations of the VDE are performed with the JOREK code (Sec. 2.1), yielding time-resolved 3D magnetic fields and plasma source terms such as parallel heat flux and halo current channels. Second, a field-line-tracing post-processor maps these plasma power and current loads onto a high-fidelity 3D model of the First Wall (FW) (Sec. 2.2). Third, for each wall element, a one-dimensional transient heat-conduction problem is solved in the wall-normal direction, using the mapped heat fluxes (Sec. 2.3). From this, the peak surface temperature is evaluated to assess whether melting occurs. Note that the wall thermal response is evaluated in post-processing, without feedback on the MHD evolution that may take place once wall erosion arises (due to release of armour material into the quenching plasma).

2.1. The JOREK MHD simulations

Except for the new JET case presented in Section 3, the MHD cases employed in this work and their underlying assumptions have already been published in [4]. The plasma is time-evolved in JOREK in the reduced-MHD approximation, coupled to the thin-wall code STARWALL to capture the plasma-vessel electromagnetic interaction. The solved variables are (ψ, Φ, j, w, T) , denoting the poloidal magnetic flux, electrostatic potential, toroidal current density, toroidal vorticity and a single temperature $(T_i = T_e = T/2)$. Impurity radiation physics and self-consistent plasma-wall interaction (beyond the plasma-vessel feedback) are not included, and ferromagnetic effects from the JET iron core are omitted. Additionally, the plasma density is constant in time and space, and the parallel main ion flow term is neglected $(v_{\parallel}=0)$. With these assumptions, the main heating source is ohmic heating and the main thermal sinks are parallel conduction and perpendicular convection.

These choices are made explicit in [4] and reproduce global JET observables (I_p, q_{95}, Z_{curr}) within experimental bounds. For ITER, the same physics model was used but with a rescaling of diffusive times to bring the very long unmitigated VDE evolution into tractable runtimes (re-scaling factor of 60). In addition, all simulations are resolved considering four toroidal Fourier harmonics $(n \in [0,3])$.

Boundary conditions and their implications for thermal loads Dirichlet boundary conditions are used for all variables except for ψ and j where the JOREK-STARWALL coupling is implemented. These simplifications result in the no flow condition ($\mathbf{v} \cdot \mathbf{n} = 0$), leading to the following heat flux form at the plasma-wall interface

$$\mathbf{q} \simeq \mathbf{q}_{\parallel} = -\kappa_{\parallel}(\overline{T}) \nabla_{\parallel} T, \qquad \overline{T} \equiv \max(T, T_{\min, \kappa_{\parallel}}),$$
 (1)

where $\kappa_{\parallel}(T)$ is the Spitzer–Härm conductivity with a floor value defined by $T_{\min,\kappa_{\parallel}}$. The Dirichlet condition for the temperature is chosen in all simulations as $T_e=1~{\rm eV}$ to suppress unrealistic halo currents that would otherwise arise in the far scrape-off layer (SOL) in regions with no ion density. To keep the resulting conductive boundary layer numerically resolvable, without artificially enhancing heat losses in the core, we set $T_{e,\min,\kappa_{\parallel}}=30~{\rm eV}$ for the evaluation of κ_{\parallel} only (i.e. note that the temperature field itself is not clipped).

At first sight, these boundary choices may appear too crude for a quantitative heat-flux study. However, the JET validation in Sec. 3 demonstrates good agreement for two discharges that span a broad range in toroidal field (B_T) , I_p , and density (n_e) . This indicates that the CQ conditions place the SOL in a conduction-limited regime, where results are insensitive to the precise wall boundary value of T_e . In a conduction-limited SOL, the relevant control parameter is the Knudsen number $\mathrm{Kn} \equiv \lambda_e/L_\parallel$, where λ_e denotes the electron collision meanfree and L_\parallel the field line connection length to the wall. Using representative CQ values from our simulations, $T_{e,\mathrm{core}} = 100 \,\mathrm{eV}$, $n_e = 8 \times 10^{19} \,\mathrm{m}^{-3}$, and $L_\parallel = 100 \,\mathrm{m}$, we find $\lambda_e \simeq 1.4 \,\mathrm{m}$ and hence $\mathrm{Kn} \approx 0.014 \ll 0.1$. This is consistent with steep parallel temperature gradients set by Spitzer–Härm conduction and weak sensitivity to the boundary condition [5]. A fully self-consistent set of boundary conditions, such as those described in [6], remains numerically intractable in JOREK for the present type of disruption simulations [4]. It is important to emphasize that partial implementation of such models is insufficient. For example, imposing sheath boundary conditions on the temperature alone still leaves the density at the plasma–wall interface as a free parameter, which can easily take higher values than pre-disruption levels [6]. If the density is instead evolved self-consistently, including effects such as neutral recycling, then sheath boundary conditions on the electric potential must also be imposed in order to prevent the formation of spurious currents in regions with no available charges.

2.2. Field line tracing

Once q_{\parallel} is obtained from the MHD simulations, it is mapped from the axisymmetric JOREK boundary to the 3D wall elements. The incident heat flux, q_{\perp} , is then computed by projecting the parallel heat flux onto the local wall-normal vector, $q_{\perp} = \mathbf{q}_{\parallel} \cdot \mathbf{n}$, but only for wall elements identified as wetted by the plasma. The wetted elements are determined via field-line tracing as performed in [1], following the same procedure as in the SMITER code: a wall element is considered wetted if its field line connects to the plasma without intersecting another within a predefined connection length. For the simulations employed in this work, the predefined minimum connection length for plasma wetting is 5 m. As a consistency check, JOREK was successfully benchmarked against SMITER for the wetted-area calculation on the same 3D CAD model of the ITER FWPs as depicted in Fig. 2.

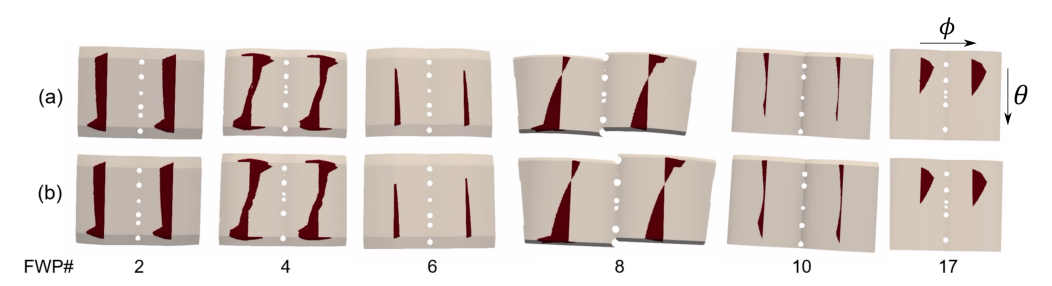


FIG. 2. Wetted area (red) calculated in SMITER (a) and JOREK (b) for 6 out of the 18 poloidally distributed FWPs for a pre-disruptive ITER X-point plasma (IMAS URI = imas:mdsplus?user=public;pulse=135011;run=7;database=ITER;version=3 at 200s).

2.3. Wall temperature evolution

For each wall element, the transient temperature evolution is obtained by solving an independent one-dimensional heat-diffusion equation along the local surface normal. This treatment is intentionally conservative: neglecting lateral (toroidal or poloidal) heat spreading tends to slightly overestimate the peak surface temperature. The thermal model employs temperature-dependent specific heat capacity and thermal conductivity for both W and Be, while the weak temperature dependence of the solid density is neglected. At the plasma-facing surface, the boundary condition prescribes the heat-flux density q_{\perp} computed in Section 2.2:

$$\left. \frac{\partial T}{\partial x} \right|_{\text{front}} = -\frac{q_{\perp}(t)}{k(T)},$$

where x is the coordinate normal to the surface and k(T) is the temperature-dependent thermal conductivity. At the rear surface, a zero-flux (thermally insulated) boundary condition $\partial T/\partial x=0$ is applied. For all simulations, a wall thickness of $12~\mathrm{mm}$ is assumed, consistent with the ITER FW armour thickness in regions expected to receive the highest disruption loads [2]. Although the Be tiles in JET are thicker, neither this difference nor the rear-side insulation assumption significantly affects the results, since the disruption duration is much shorter than the characteristic thermal diffusion time through the material. As a consistency check, the numerical solver was verified against the analytical solution for a fast, constant heat pulse in the semi-infinite slab approximation, yielding excellent agreement.

3. MODEL VALIDATION IN JET VDES

In this section we apply the workflow detailed in Section 2 to two different JET unmitigated upward-going, VDEs, namely pulse numbers #95110 and #84832 described in [7], with pre-disruption I_p , B_T , and n_e of (1.1 MA, 1.2 T, 1.5×10^{19} m⁻³) and (2.2 MA, 2.2 T, 8.0×10^{19} m⁻³) respectively.

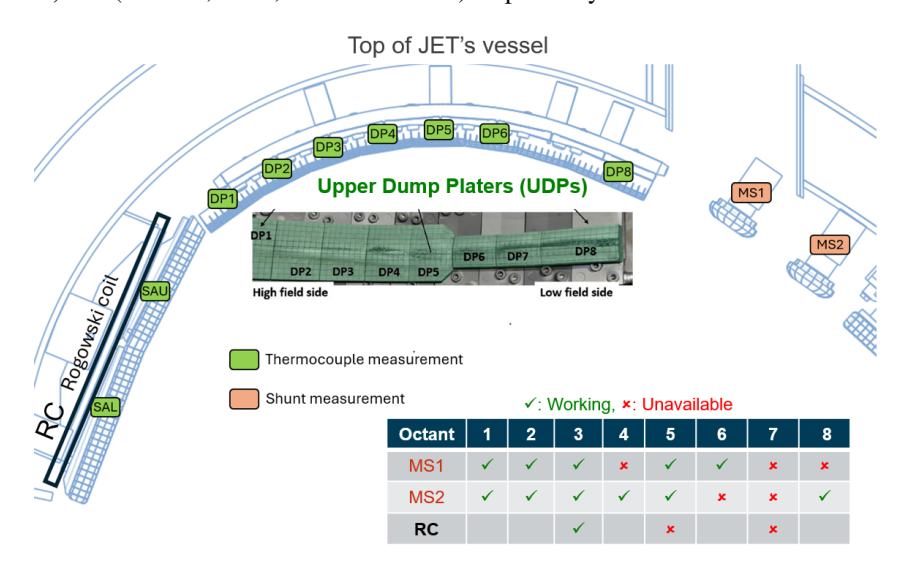


FIG. 3. Summary of the JET diagnostics used for thermal loads and halo currents in this study. Green boxes denote TC measurements while light-red boxes denote shunt measurements (MS1/2). The black and thick rectangular outline shows a Rogowski coil (RC) and the bottom table shows the toroidal coverage and availability for halo current measurements in each of the JET octants for the considered shots.

3.1. Measurement diagnostics in JET

Measurements of the I_p , the current-centroid position, and their toroidal asymmetries are obtained using the magnetic diagnostics and analysis methods described in [8], which were also employed for comparison with JOREK simulations in [4]. For the thermal load analysis, subsurface thermocouples (TC) are located in the Be Upper Dump Plates (UDP) and in the Be upper inner-wall protection limiters ("sausage" limiters, SAU/SAL). The UDP TCs are located in Octant 2, whereas the sausage-limiters TCs are located in Octant 1. The poloidal positions of the TC can be seen in Fig 3. Because unmitigated VDEs are toroidally asymmetric [8], measurements from a single toroidal sector can be misleading. To assess the degree of toroidal asymmetry, we also use halo-current data from the so-called "mushroom" shunt (MS) diagnostics, also shown in Fig. 3. These shunts are installed in several octants, although some channels are unavailable for the pulses modelled here due to technical issues. Since halo currents and parallel heat fluxes to the wall are both driven by the same MHD and connection-length geometry, a correlation between the two is expected. The shunt signals therefore provide a proxy for the toroidal distribution (and effective width) of the heat deposition in regions not instrumented with TCs.

The TCs are used to reconstruct the total energy deposited on the PFCs using the calorimetric inversion procedure described in [9]. Although the UDPs are instrumented with subsurface TCs, the calorimetric analysis requires internal thermal equilibrium within the tile volume, using long tile cooling times for fitting. As a result, the inferred energy deposition cannot be separated into pre-disruptive and disruption deposited energy with this method. To isolate the disruption contribution, we subtract the energy measured in a reference discharge that is either non-disruptive or strongly mitigated. For discharge #95110, the reference is #95108 [7], in which a neon

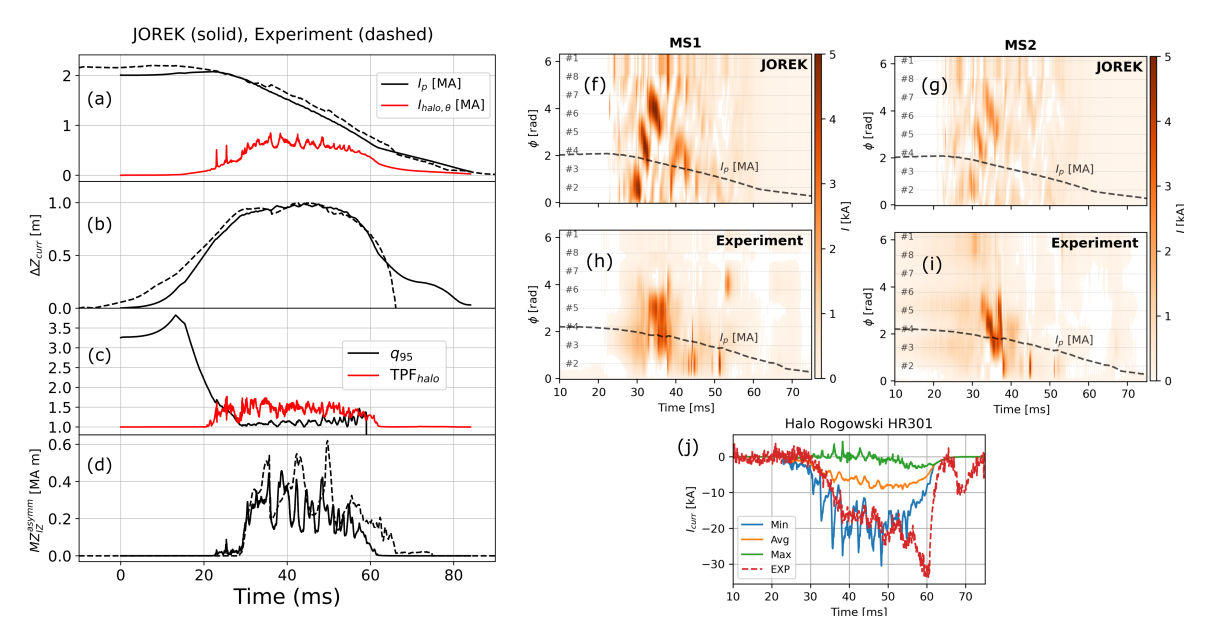


FIG. 4. (Left) Comparison of simulated values (solid) with experimental values (dashed) for shot #84832. (a) Plasma current and poloidal halo currents. (b) Vertical displacement of the current-centroid. (c) Edge safety factor and toroidal peaking factor of the poloidal halo currents. (d) n=1 asymmetry of the vertical current moment as defined in [8]. (Right) Toroidal current distribution measured by the mushroom shunts MS1 (f,h) and MS1 (g,i) in JOREK (f,g) and in the experiment (h,i). The indices (e.g. #8) show the octant on which the measurement is taken. Panel (j) shows the halo current measured by Rogowski coil HR301 (dashed red) and the minimum, average, and maximum currents obtained from a set of equivalent toroidally distributed coils in JOREK.

shattered pellet was injected prior to the VDE. For #84832, the reference is the non-disruptive shot with very similar characteristics (#85364).

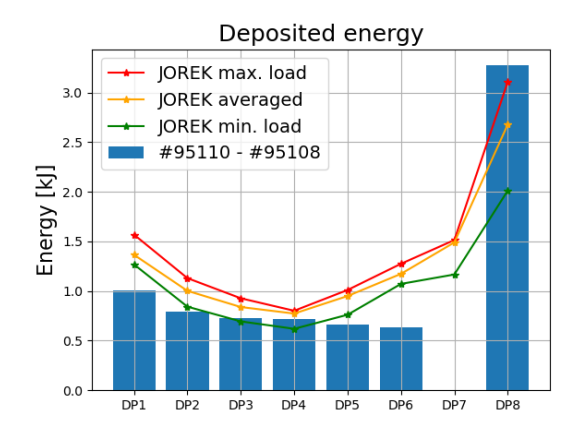
3.2. MHD simulation for discharge #84832

JET discharge #84832 has been simulated with JOREK using the same physics model and numerical parameters as for discharge #95110 [4]. Experimentally, this pulse underwent an H-L back-transition followed by a loss of vertical stability [7]. In contrast to #95110, discharge #84832 produced melting of the UDPs and visible release of Be droplets [10]. This can be attributed to the substantially higher stored energies: the magnetic energy was about four times larger, and the pre-TQ thermal energy was 2.2 MJ compared to only 0.21 MJ in #95110. These features make #84832 a particularly relevant case for assessing thermal loads.

Figures 4 (a–d) compares key global quantities between simulation and experiment: I_p , the vertical position of the current centroid, and the n=1 asymmetry of the vertical current moment (as defined in Ref. [8]). In all cases, the simulated evolution follows the experimental trends closely, giving confidence in the modelled global dynamics. The toroidal distribution of halo currents is shown in Fig. 4 (f–i), where the mushroom shunt measurements are compared with the field-line–tracing calculation from JOREK. The simulations capture both the sign and magnitude of the measured currents, although the toroidal pattern in JOREK exhibits additional rotation (one full turn instead of a half turn). The direction of this rotation differs from the experiment and will require further investigation. Finally, Fig. 4 (j) compares the halo current measured by the Rogowski coil HR301 with the range of values obtained from a set of virtual toroidally distributed coils in JOREK. The simulated signals reproduce the experimental magnitude when the toroidal sector corresponding to the minimum current is considered.

3.3. Thermal load analysis

Following the workflow described in Sec. 2 and the experimental set-up in Sec. 3.1, the deposited energies in the UDPs for both discharges are shown in Fig. 5. The total radiation fraction during the TQ and CQ phases, estimated from the vertical bolometer (KB5V) camera, is $f_{\rm rad}=28\%$ for #95110 and 22% for #84832. Since radiation cooling is not included in the JOREK simulations, the computed heat fluxes have been rescaled by a factor $(1-f_{\rm rad})$ for a consistent comparison. The different JOREK lines in Fig. 5 correspond to toroidal locations where the total energy deposited on the UDPs reaches its maximum and minimum and its average value.



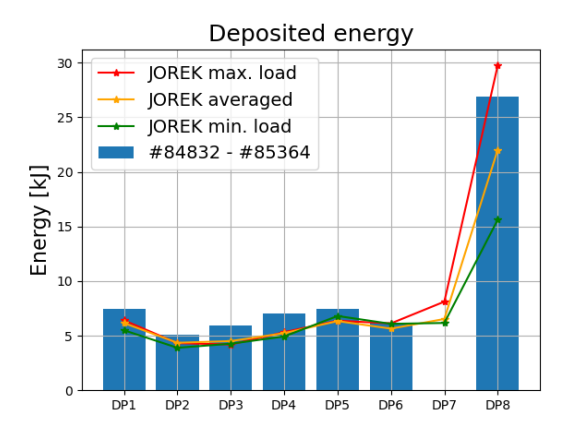


FIG. 5. Energy deposited on the UDPs as measured by the JET TCs using the reference pulse subtraction method explained in Sec. 3.1 (blue bars) and that calculated in the JOREK simulations (colored lines) for #95110 (left) and #84832 (right). The different simulation lines correspond to the toroidal locations with minimum, average, and maximum deposited energy in the totality of the UDPs obtained in JOREK. Note that the JOREK results have been scaled down by a factor $(1-f_{rad})$ to account for the radiation losses in the experiment which are not modeled by JOREK. The error in the estimations of the deposited energy is expected to be <20% [9].

The results indicate that toroidal asymmetries in the deposited energy are on the order of $\sim 20\%$. The largest asymmetry is found in UDP 8, caused primarily by the TQ phase, which concentrates most of its thermal energy deposition on that plate.

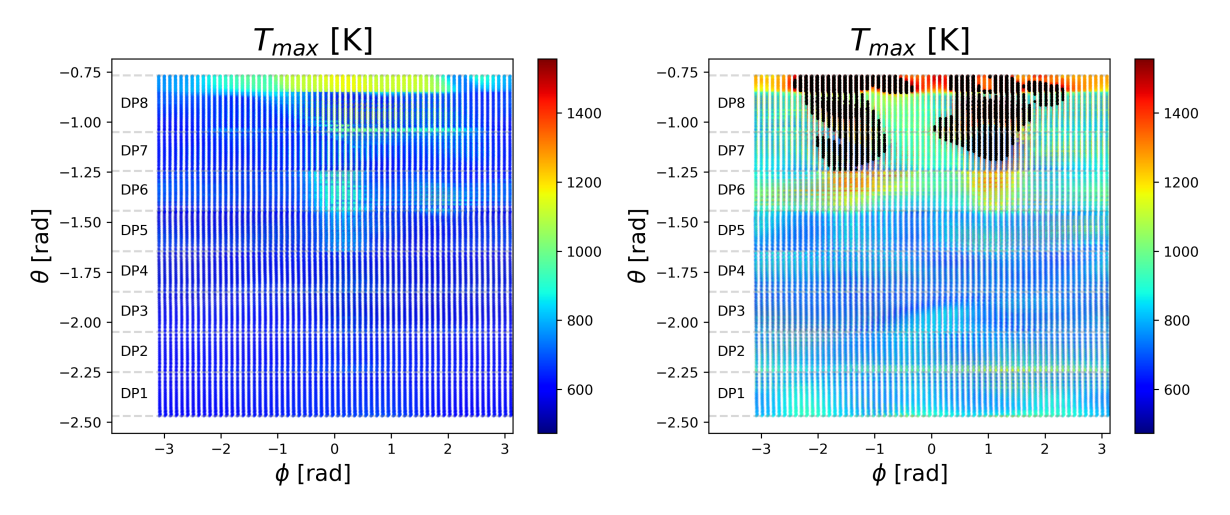


FIG. 6. Maximum surface temperature on the JET UDPs as predicted by JOREK for #95110 (left) and (right) #84832. The plates are displayed in toroidal (ϕ) and poloidal (θ) angles and the black dots represent elements with temperatures beyond the melting point of Be (1556 K).

Starting with a pre-disruptive wall temperature of 200°C for this discharge [10], Fig. 6 shows the maximum surface temperature reached in the JET UDPs as predicted by the JOREK heat-flux calculations. For discharge #95110 (left), no melting is predicted, consistent with the absence of visible melt damage in the experiment. In contrast, for discharge #84832 (right), melting of Be is predicted in UDPs 7 and 8 (black points), in agreement with the experimental observation of molten Be release in this region [10]. The longest predicted melting duration occurs on UDP 8, where the surface remains above the Be melt temperature (1556 K) for approximately 6 ms.

A more detailed analysis shows that, for #84832, neither the TQ nor the CQ phase alone is sufficient to produce significant melting. Considering only the TQ fluxes yields at most mild surface melting, with a duration below 0.6 ms, while the CQ loads alone do not raise the surface temperature above the melt point. Melting is obtained *only* when both phases are combined: the TQ acts to pre-heat the PFC surface, and the subsequent CQ heat loads then sustain and further increase the surface temperature. As also discussed in [11], this illustrates the importance of capturing the combined action of both disruption phases for accurate melt predictions.

4. PREDICTION FOR A HIGH CURRENT ITER VDE

Having established a reasonably successful validation of the modelling workflow against dedicated JET VDE experiments in Sec. 3, we now turn to predictions for ITER. We focus on an unmitigated upward-going VDE simulated with JOREK, which corresponds to the case with a CQ duration of 240 ms in Ref. [4]. This case represents the maximum magnetic energy content of ITER disruptions, since it assumes the maximum $I_p=15\,\mathrm{MA}$. At the same time, this is an L-mode plasma and the pre-TQ thermal energy is modest, about 30 MJ, which is much smaller than the $\sim350\,\mathrm{MJ}$ of thermal energy stored in a fully developed $Q=10\,\mathrm{H}$ -mode scenario. Consequently, the results presented here should be regarded as a worst-case scenario for CQ-induced thermal loads, but not for TQ loads. The latter could be considerably more severe in the event of a loss of vertical control in a fully developed $Q=10\,\mathrm{plasma}$ without disruption mitigation — a situation that is expected to be extremely rare during ITER operation.

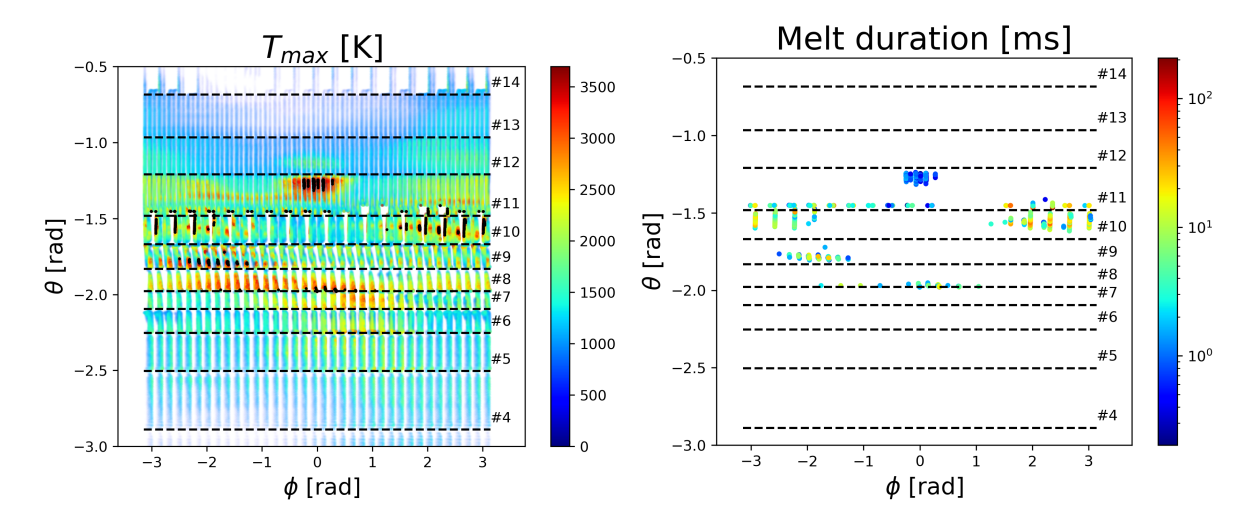


FIG. 7. Maximum surface temperature (left) and melt duration (right) on the ITER FW during a 15 MA unmitigated upward VDE. The FW surface is represented in toroidal (ϕ) and poloidal (θ) coordinates, with the poloidal index of the FW panels (#). Black dots mark elements where the surface temperature exceeds the W melting point.

Figure 7 (left) presents the maximum surface temperature attained during the disruption, assuming a pre-disruptive wall temperature of 500° C (expected to be reasonable during burning plasma operation on the FWPs). The map is subdivided into individual FWPs for reference. The first instances of melting appear during the TQ, which lasts about 6 ms, affecting FWP #11. However, in this case the surface remains above the melting threshold of W for only ~ 2 ms, as shown in Fig. 7 (right). As the CQ proceeds and the plasma column drifts upward, the load shifts progressively towards higher panel rows (with FWP #8 being the uppermost). The most pronounced melting is predicted on FWP #10, with melt durations reaching several tens of milliseconds. Importantly, these events are not located on the main areas of the panel surfaces, but rather near the panel edges where the local incidence angle between field lines and the wall normal becomes nearly perpendicular (due to the stronger toroidal shaping in the panel wings). Such conditions occur on FWPs #10 and #11, where the open geometry around the ITER upper ports allows deeper penetration of magnetic field lines. This issue is already being considered by the ITER FW design team in order to minimize edge loading effects. During the CQ, most of the thermal energy is deposited on the top-row panels (FWPs #7, 8, and 9). In these regions, the toroidal asymmetry of the deposition remains below a factor of two. Only localized melting is observed in these panels, with durations typically below 20 ms.

5. CONCLUSIONS AND OUTLOOK

We have combined MHD simulations, field-line tracing on a realistic 3D wall, and a transient wall thermal response model to study unmitigated VDEs in JET and ITER. Validation against two dedicated JET discharges shows that the simulations reproduce the global evolution of the plasma current, current-centroid motion, current asymmetries and yield reasonable agreement with thermocouple-inferred energy deposition. Although boundary conditions are simplified, the CQ appears to be conduction-limited, which reduces sensitivity to such simplifications. Consistent with experiment, melting is predicted for the high-current JET case and not for the lower-current case; crucially, the melting requires the combined action of the TQ and CQ, with the TQ preheating the sur-

face and the CQ sustaining and amplifying the temperature rise. These validated heat-load cases may provide physics-based inputs for dedicated melt-motion modelling (e.g. MEMENTO [12]).

Applying the workflow to ITER, we considered a 15 MA unmitigated upward VDE with a 240 ms CQ. The main chamber W FWPs experience only marginal melting with short durations, whereas more substantial melting (which can reach melt durations of several tens of milliseconds) is localized to exposed panel edges near the upper ports where field lines intersect the wall at near-normal incidence. Toroidal plasma asymmetries amplify local peak surface temperatures relative to axisymmetric assumptions by up to a factor of 2 during the CQ and 3 during the TQ, highlighting the need for fully 3D treatments. At the same time, the MHD dynamics broaden the heat-flux profiles compared with axisymmetric transport/equilibrium workflows (e.g. DINA and TOKES), which would otherwise over-localize the loads. For example, 2D TOKES simulations for the W FWPs predicted CQ melting already at 10 MA considering a fixed equilibrium and poloidal energy deposition width $\lambda_E=3.5$ cm. Despite a two-fold increase in energy (15 MA) and toroidal localization, the JOREK simulations show marginal melting due to the moving equilibrium and MHD spreading, leading to much broader λ_E in the range of tens of cm. Overall, this state-of-the-art workflow highlights that the ITER W FW is markedly more resilient to disruption heat loads than the previous Be armoured wall, easing CQ thermal-mitigation requirements. Because radiation and impurity effects are neglected here, the reported temperatures and melt durations may also be regarded as conservative.

Future work should extend the physics fidelity of the JOREK simulations by including radiation and impurity, refining boundary conditions (sheath physics and density evolution), and exploring TQ-dominated scenarios with higher thermal energies. Coupling the present heat-load predictions to melt-evolution solvers will enable assessments of melt-layer motion, droplet ejection, and lifetime impacts. TOKES simulations of the TQ with input guided by these results, have been produced and will be reported in a forthcoming publication. The impact of W evaporation and plasma radiation as a self-mitigation mechanism can also be investigated with TOKES.

ACKNOWLEDGEMENTS

ITER is the Nuclear Facility INB No. 174. This work explores the physics processes during plasma operation of the tokamak when disruptions take place; nevertheless the nuclear operator is not constrained by the results presented here. This work has been carried out within the framework of the EUROfusion Consortium, funded by the European Union via the Euratom Research and Training Programme (Grant Agreement No 101052200 — EUROfusion). Views and opinions expressed are however those of the author(s) only and do not necessarily reflect those of the European Union, the European Commission or the ITER Organization. Neither the of these institutions can be held responsible for them.

REFERENCES

- [1] COBURN, J. et al, Nucl. Fusion 62 (2022) 016001.
- [2] PITTS, R.A. et al, Nucl. Fusion 42 (2025) 101854.
- [3] PITTS, R.A., TOKES simulations of first wall and divertor damage during unmitigated disruptions on ITER, IAEA-CN-316-2152, presented at the 29th Fusion Energy Conference, UK, 2023.
- [4] ARTOLA, F.J. et al, Plasma Physics and Controlled Fusion 66 (2024) 055015.
- [5] STANGEBY, P.C., The Plasma Boundary of Magnetic Fusion Devices, Taylor & Francis Group, Great Britain (2000).
- [6] ARTOLA, F.J. et al, PPCF 63 (2021) 064004.
- [7] GERASIMOV, S.N. et al, Phys. Scr. 99 (2024) 075615
- [8] GERASIMOV, S.N. et al, Nucl. Fusion 54 (2014) 073009.
- [9] MATTHEWS, G.F. et al, Journal of Nuclear Materials 12 (2017) 227-233.
- [10] JEPU, I. et al, Nucl. Fusion 59 (2019) 086009.
- [11] RANTYNSKAIA, S. et al, Nucl. Fusion 60 (2020) 104001.
- [12] PASCHALIDIS, K. et al, Journal of Nuclear Materials 206 (2024) 114603.